HHS Public Access
Author manuscript
Med Image Anal. Author manuscript; available in PMC 2016 December 01.

Published in final edited form as:
Med Image Anal. 2015 December ; 26(1): 217–231. doi:10.1016/j.media.2015.09.003.

Medially constrained deformable modeling for segmentation of branching medial structures: Application to aortic valve segmentation and morphometry

Alison M. Pouch[1,2], **Sijie Tian**[2], **Manabu Takebe**[2], **Jiefu Yuan**[2], **Robert Gorman Jr.**[2], **Albert T. Cheung**[3], **Hongzhi Wang**[4], **Benjamin Jackson**[1], **Joseph H. Gorman III**[1,2], **Robert C. Gorman**[1,2], and **Paul A. Yushkevich**[5]

[1]Deparment of Surgery, University of Pennsylvania, Philadelphia, PA

[2]Gorman Cardiovascular Research Group, University of Pennsylvania, Philadelphia, PA

[3]Deparment of Anesthesiology, Perioperative, and Pain Medicine, Stanford University, Stanford, CA

[4]IBM Almaden Research Center, San Jose, CA

[5]Department of Radiology, University of Pennsylvania, Philadelphia, PA

Abstract

Deformable modeling with medial axis representation is a useful means of segmenting and parametrically describing the shape of anatomical structures in medical images. Continuous medial representation (cm-rep) is a “skeleton-first” approach to deformable medial modeling that explicitly parameterizes an object’s medial axis and derives the object’s boundary algorithmically. Although cm-rep has effectively been used to segment and model a number of anatomical structures with non-branching medial topologies, the framework is challenging to apply to objects with branching medial geometries since branch curves in the medial axis are difficult to parameterize. In this work, we demonstrate the first clinical application of a new “boundary-first” deformable medial modeling paradigm, wherein an object’s boundary is explicitly described and constraints are imposed on boundary geometry to preserve the branching configuration of the medial axis during model deformation. This “boundary-first” framework is leveraged to segment and morphologically analyze the aortic valve apparatus in 3D echocardiographic images. Relative to manual tracing, segmentation with deformable medial modeling achieves a mean boundary error of 0.41 ± 0.10 mm (approximately one voxel) in 22 3DE images of normal aortic valves at systole. Deformable medial modeling is additionally demonstrated on pathological cases, including aortic stenosis, Marfan syndrome, and bicuspid aortic valve disease. This study demonstrates a promising approach for quantitative 3DE analysis of aortic valve morphology.

Corresponding Author: Alison M. Pouch, Ph.D., Smilow Center for Translational Research, University of Pennsylvania, 3400 Civic Center Boulevard, Building 421, 11th Floor, Room 112, Philadelphia, PA 19104, pouch@seas.upenn.edu, Phone: 215-837-4896.

Graphical Abstract

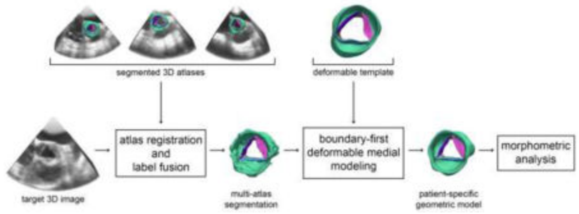

Keywords

image segmentation; deformable modeling; medial axis representation; branching medial model; aortic valve; 3D echocardiography

1. INTRODUCTION

1.1. Deformable modeling of heart valves in 3D echocardiographic images

Echocardiography is the most commonly used imaging modality for the evaluation of heart valve disease. Image segmentation of heart valves in 3D echocardiographic (3DE) data is a means of extracting visual and quantitative information about patient-specific in vivo valve morphology that can support valve diagnostics and surgical treatment planning (Jassar et al., 2014, Noack et al., 2013, Veronesi et al., 2009, Vergnat et al., 2011). Image segmentation in this context, however, is difficult due to the signal dropouts and noise that are characteristic of echocardiographic imaging, as well as the fact that many clinically relevant valve landmarks are defined geometrically rather than by distinctive image intensity characteristics. For example, several components of the aortic valve complex, such as the sinotubular junction (STJ), the commissures, and the attachments of the aortic cusps, are identified anatomically rather than by distinctive image intensity patterns. Given these challenges, shape-guided deformable modeling methods are well suited for 3DE heart valve segmentation. Deformable modeling methods capture the geometry of an image region by deforming parametric surfaces under the influence of external data-driven forces and internal regularization forces. Shape constraints imposed on the deformable model can fill in areas of intensity inhomogeneity or establish boundaries between anatomical components that are not demarcated by image gradients. Once a parametric model of the valve is obtained, it can be interactively visualized, quantitatively analyzed, and statistically compared to other valve geometries.

Several deformable modeling methods for heart valve segmentation in 3DE images have been proposed, each of which uses a different means of representing valve shape. Ionasec et al. (2010) developed a fully automatic technique for segmenting the aortic and mitral valves in 3DE images. Given a database of manually landmarked images, machine learning algorithms globally locate and track several valve landmarks throughout the cardiac cycle. Spline surfaces are fitted through these points with the aid of learned boundary detectors to represent the geometry of the valves. In other work, Schneider et al. (2011) present a deformable model-based 4D segmentation of the mitral leaflets in real-time 3DE data in which the leaflets are represented with a triangulated mesh. Once the leaflets are segmented at diastole, the mesh deforms to subsequent time points in the cardiac cycle under the influence of multiple image-driven and regularizing forces. The regularizing forces encourage leaflet stretching during valve closure, prevent excessive leaflet bending and collision, and encourage the leaflet free edges to point into the left ventricle. This segmentation and deformable modeling method has only been applied to the mitral valve and has not yet been extended to the aortic valve.

Our earlier work (Pouch et al., 2013, 2014) differs from the above deformable modeling methods in that it represents mitral and aortic leaflet geometry volumetrically, i.e. as structures with locally varying thickness. The shape descriptor we use for the deformable model is 3D continuous medial representation, or cm-rep (Yushkevich et al., 2006a). This representation describes the relationship between the surfaces and the interior, or morphological skeleton[1], of the leaflets. In (1967), Blum introduced the notion of the medial axis in 2D as a means of shape classification and discrimination for biological problems. The definition naturally extends to 3D, as described in Section 2.1, and has been leveraged for parametric deformable modeling of anatomical structures in medical images. Deformable models based on the medial representation were pioneered by Pizer et al. (1999, 2003, 2013) and have two particular advantages in medical image segmentation and shape analysis: they can be used to constrain the branching configuration of the segmented anatomical structure, and they can be used to statistically compare skeleton-derived shape features in a population of instances of those segmented anatomical structures. In the continuous medial representation (cm-rep) framework described in (Yushkevich et al. 2006a), a deformable model represents an object's medial axis as a parametric surface, and the thickness of the object at each point on the medial axis is also parametrically defined. This is in contrast to the original medial representation of Pizer et al. (2003), in which the medial axis is described using a discrete set of primitives, or "atoms". The parametric description of the skeleton as a surface with thickness can be "inflated" using a simple analytical expression to form a volumetric representation of the object, a process referred to as *inverse skeletonization*. (Note that since the object's boundary is derived from the object's skeleton, the cm-rep method is considered a "skeleton-first" approach to medial representation.) By modifying the parameters of the skeleton, the cm-rep model can be deformed to take on new shapes. Gradient-based optimization schemes can be applied to the model parameters in order to deform the model to approximate the shape of anatomical structures in 3D image data. Typically, these structures are first segmented using some separate segmentation algorithm, and the cm-rep model is fitted to the binary or multi-label segmentation of the structure of interest (Yushkevich et al., 2006a, 2008; Pouch et al. 2014). However, the optimization can also be formulated to fit the model directly to image intensities, as in (Sun et al., 2010). The motivation for using cm-rep as a shape descriptor for heart valve leaflets is that it is useful for volumetric modeling of thin sheet-like structures. The parametric model explicitly defines leaflet thickness, which is an important tissue parameter in biomechanical valve simulation (Rausch et al., 2012) and may be indicative of valve pathology, such as calcification or degenerative processes. Moreover, the aortic and ventricular surfaces of the

[1]Note that in this work, the terms medial axis and morphological skeleton are used interchangeably when referring to either 2D or 3D objects. The medial axis of a 2D object is a set of curves, and the medial axis of a 3D object is generically a set of surfaces. We also use the term medial scaffold to specifically refer to a 3D medial axis or skeleton.

aortic cusps are both delineated, and constraints on medial geometry prevent these surfaces from intersecting during model deformation.

1.2. Challenges of deformable modeling of the aortic valve apparatus with medial axis representation

A major limitation of the cm-rep method described above is that it is limited to modeling 3D structures that can be accurately represented using a single-surface medial axis. However, many sheet-like anatomical structure can only be described using a medial axis consisting of multiple adjoining surfaces, or “branches.” So, while cm-rep has been effectively used to describe mitral and aortic leaflet morphology in 3DE images, applying it to the entire aortic valve complex (including the sinuses of Valsalva) is not possible. The heart valve leaflets themselves can be described in terms of a single non-branching medial manifold; however, the entire aortic valve complex has a branching medial representation, as illustrated in Fig. 1. The aortic root, extending from the left ventricular outlet (LVO) to the STJ, can be modeled with a single medial manifold in the absence of the aortic cusps, as in Fig. 1a. The aortic cusps can likewise be modeled as individual medial manifolds (Fig. 1b, blue surfaces), but the entire valve apparatus is a branching medial model where the cusps attach to the aortic root at seams, or branch curves, in the medial scaffold. The cm-rep methodology has the limitation that medial axes are difficult to explicitly parameterize along curves at which medial surfaces meet. For example, the inverse skeletonization equations that are used to obtain a volumetric representation from an object’s medial axis (Yushkevich et al., 2006a) are asymptotic at the edges of the medial axis and along branch curves in the medial axis. Work that extends the cm-rep paradigm to medial axes with multiple branches has been very limited. Terriberry and Gerig (2006) proposed a special spline-based representation that allows parametric representation of seam curves and demonstrates it in a toy example, but this method has never been shown to work in actual anatomical structures or in the context of deformable modeling. Sun et al. (2010) proposes a cm-rep model with seams and uses it to model the myocardium, but their model cannot handle seam-edge curve junctions and is thus limited to a very special class of anatomical modeling problems. In the original m-rep framework (Pizer et al., 2003), complex structures whose medial axis has multiple branches are approximated using a union of single-branch m-rep “figures” enveloped by a shrink-wrapped surface. While such a representation is versatile, it deviates from the actual 3D geometry of medial axes (i.e. the true medial axis of the shrink-wrapped surface can be completely different from the skeletons of the two component figures). In this work, as in the cm-rep method, our goal is to use 3D medial representations that are faithful to the medial geometry described by Blum and others.

Section 1.3. Representation of the aortic valve apparatus with a medially constrained boundary-first deformable model

To overcome the challenge of modeling structures with branching medial topologies, a novel “boundary-first” deformable medial modeling paradigm was recently proposed (Yushkevich et al., 2013). Rather than explicitly parameterizing a structure’s medial axis and determining its boundary algorithmically as is done with “skeleton-first” cm-rep, the boundary-first strategy explicitly describes the model’s boundary and implicitly maintains medial axis topology by imposing geometric constraints on the boundary of the model as it deforms.

Since these constraints are nearly identical at the interior of the medial axis and along branch curves, the framework supports medial modeling of structures with branching medial axes while adhering to the medial axis definition described in (Blum, 1967). To date, the feasibility of modeling branching structures with this boundary-first paradigm has only been demonstrated with a toy example and has not been translated to real-world applications. The contribution of the present work is to leverage this paradigm for segmentation, geometrical modeling, and quantitative analysis of the aortic valve in 3DE images[2], a schematic of which is presented in Fig. 2. First, the aortic valve apparatus is segmented in a target 3DE image using multi-atlas label fusion. Then a boundary-first deformable medial model is fitted to the result of multi-atlas segmentation, and clinically relevant measurements of valve morphology are computed. It is worth noting that if multi-atlas segmentation were performed alone without the use of deformable medial modeling, it would be challenging to reliably extract clinically relevant geometrical features of the aortic valve apparatus, such as the crown-shaped annular contour. The multi-atlas segmentation simply assigns an anatomical label to each image voxel without offering a parametric representation of the segmented structures or even guaranteeing the topology of these structures. Thus, multi-atlas segmentation alone cannot yield locally varying thickness measurements, automatically identify landmarks such as the commissures, establish correspondences on valves of different subjects, or ensure topological consistency of different instances of the valve. Fitting deformable medial models to different instances of the aortic valve imposes a common shape-based coordinate system on those instances that allows for shape comparison and straightforward extraction of clinically relevant measurements. Therefore, the advantage of combining medial modeling with multi-atlas segmentation is that deformable medial modeling facilitates landmark identification, quantitative morphometry, and statistical shape analysis. Our work conceptually demonstrates that deformable medial modeling is not limited to anatomical structures with simple shape; it is potentially applicable to a vast range of clinical problems that involve anatomical structures with complex geometries.

This paper is outlined as follows. Section 2 describes the concept of deformable medial modeling and the difference between the skeleton-first and boundary-first paradigms. It introduces the 3D medial geometry of the aortic valve complex and how a deformable model of the aortic apparatus is generated and fitted to 3DE image data. Section 3 describes experiments in which boundary-first cm-rep is used to segment the aortic valve complex in 3DE images and clinically relevant measurements are derived from the deformable model. Section 4 presents the results of automated aortic valve segmentation in subjects with normal aortic valve morphology and demonstrates the method's ability to capture aortic valve pathology. The paper concludes with a discussion in Section 5.

[2]Preliminary results of aortic valve segmentation using boundary-first deformable medial modeling are presented in Pouch et al., 2015. The present work differs in that it includes a larger patient population, has more detailed methodological description, reports the accuracy of clinically relevant measurements of aortic valve geometry, and includes examples of pathological aortic valve morphologies.

2. METHODS

2.1. The medial axis transform and general approaches to deformable medial modeling

The medial axis transform (*MAT*), whose use as a shape descriptor was pioneered by Blum in (1967), was originally defined in 2D as the set of connected curves formed by the centers of maximally inscribed disks in the object. Blum's 2D definition of the *MAT* is easily extended to 3D, where an object's medial axis is a scaffold, or a set of connected surfaces formed by the centers of maximally inscribed balls (MIBs) of the object, where a ball refers to the generalization of a disc to higher dimensions (i.e. a sphere and its interior). More formally, suppose an object is represented by the set $S \subset \mathbb{R}^N$ with a smooth boundary denoted by ∂S. Then $MAT(S)$ is a mapping between points on ∂S and points on S that are centers of the MIBs of S, where a MIB is defined as a ball $B \subset S$ that satisfies the condition that there exists no other ball $B' \subset S$ such that $B \subset B'$. In other words, if S is a 3D object, $MAT(S)$ can be defined by the set of parameters $\{\mathbf{m}, R\}$, where $\mathbf{m} \in \mathbb{R}^3$ is the set of the centers of the MIBs of S and $R \in \mathbb{R}^+$ refers to the radius of the corresponding MIBs.

There are two approaches to deformable modeling that use medial geometry as a means of shape representation. Illustratively compared in Fig. 3, these approaches use different strategies of constraining the deformable model to maintain a consistent medial geometry. (Note that Fig. 3 is presented in 2D for demonstrative purposes, but medial modeling described in this work is performed entirely in 3D.) The skeleton-first approach, which is exemplified by the cm-rep approach (Yushkevich et al., 2006a) as well as the m-rep/s-rep approaches (Pizer et al., 1999, 2013), explicitly parameterizes the medial axis of the deformable model and derives its boundary as a function of the medial axis. As shown in Fig. 3a–b, the cm-rep deformable model is defined in terms of a set of coefficients (e.g., spline control points) that describe a parametric skeleton manifold $\mathbf{m}$ and a parametric radius function R along that manifold. The model's boundary (dashed black curve in Fig. 3c) is obtained by "inflating" the skeleton. In more precise terms, the boundary is the envelope of the parametric family of balls centered along $\mathbf{m}$ with radii R, and is given by an analytic expression involving the first derivatives of $\mathbf{m}$ and R (Yushkevich et al., 2006a). During model deformation, the coefficients controlling $\mathbf{m}$ and R are updated iteratively to allow the model to capture the geometry of a target shape. While this strategy has been used in various 3D medical imaging applications (Pizer et al., 2003, Styner et al., 2003, Bouix et al., 2005, Yushkevich et al., 2008), the method has largely been limited to modeling anatomical structures with a shape simple enough to be modeled using a single manifold skeleton (e.g., hippocampus, heart valve leaflets). To accurately represent more complex shapes (like the entire aortic valve apparatus including the sinuses and cusps) the model must have a branching skeleton consisting of multiple manifolds that join along curves. Explicitly parameterizing branching medial manifolds has proven a challenge in the cm-rep framework due to the presence of complex geometrical constraints that must be satisfied by $\mathbf{m}$ and R along the curves where branches meet and at the endpoints of these curves.

The alternative boundary-first deformable medial modeling approach employed in this paper is illustrated in Fig. 3d–f. Here, the boundary of the deformable model is explicitly parameterized, and the model's medial axis geometry is implicitly encoded through the concept of “medial links”. Two or more points on the model’s boundary are medially linked if they belong to the same MIB. In Fig. 3e, the boundary points $\mathbf{x}_1$ and $\mathbf{x}_2$ are medially linked, and so are points $\mathbf{y}_1$, $\mathbf{y}_2$, and $\mathbf{y}_3$. During model deformation, the boundary is constrained to deform in ways that preserve the medial links between boundary points. In other words, the boundary is only allowed to deform in ways that keep points $\mathbf{x}_1$ and $\mathbf{x}_2$ as part of the same MIB (and likewise for points $\mathbf{y}_1$, $\mathbf{y}_2$, and $\mathbf{y}_3$), which prevents topological changes in the object’s medial axis. The model’s medial axis (dashed black curve, Fig. 3f) can be derived easily from the medial linkages. Note that for the shape shown in Fig. 3d–f, a boundary point can be linked to one, two, or no other boundary points based on its relationship to the medial axis. For example, $\mathbf{x}_1$ and $\mathbf{x}_2$ are linked since they lie on a MIB centered on the interior of the medial axis; $\mathbf{y}_1$, $\mathbf{y}_2$, and $\mathbf{y}_3$ are linked because they lie on a MIB centered on a branch point on the medial axis; and $\mathbf{z}_1$ is not linked to another boundary point since it lies on a MIB centered at an edge of the medial axis. Here, the edge of the medial axis refers to points that are on the edge of the medial curve or surface. Branch points occur where two or more medial curves or surfaces meet. The interior of the medial axis refers to points on a medial curve or surface that are not edge or branch points.

The advantage of the boundary-first approach to deformable medial modeling illustrated in Fig. 3d–f is that the medial linkage constraints that enforce valid medial geometry have a very similar formulation everywhere on the medial axis (the interior of medial surfaces, edge and seam curves, and their endpoints and intersections). This is in contrast to the cm-rep methodology (Yushkevich et al., 2008), in which special equality constraints must be imposed on the deformable model along the edge and seam curves to ensure that inverse skeletonization yields a valid surface, with even more complex (and not fully understood) constraints needed to properly model seam endpoints and seam-seam intersections (Terriberry and Gerig, 2006). Hence the boundary-first paradigm accommodates deformable medial modeling of complex, multi-component structures. However, until now, the ability of the boundary-first approach to model branching structures has not been demonstrated in real-world medical imaging data, but only in a single toy example (Yushkevich et al., 2013).

2.2. Background on boundary-first deformable medial modeling

As described in Section 2.1, the boundary-first deformable medial modeling framework explicitly parameterizes an object’s boundary, and the *MAT* of the object’s shape is encoded by grouping tuples of medially linked boundary points. Constraints imposed during model deformation ensure that these medial links are maintained. *This strategy to medial modeling leverages the fact that transformations of the object that preserve all medial links in the object also preserve the branching structure of the object’s skeleton* (Yushkevich et al., 2013, Theorem 1).

Formally, points $\mathbf{x}_1 \ldots \mathbf{x}_k \in \partial S$ are said to be medially linked if there exists a MIB $B \subset S$, such that $\mathbf{x}_1 \in B, \ldots, \mathbf{x}_k \in B$. Let R be the radius of B. Then the center of B is given by $\mathbf{x}_1 - R\mathbf{N}_1 = \mathbf{x}_2 - R\mathbf{N}_2 = \ldots = \mathbf{x}_k - R\mathbf{N}_k$, where $\mathbf{N}_1 \ldots \mathbf{N}_k$ are the unit outward normals to ∂S at $\mathbf{x}_1 \ldots \mathbf{x}_k$. Notice from the above definition that if $\mathbf{x}_1$, $\mathbf{x}_2$, $\mathbf{x}_3$ are medially linked, then $\mathbf{x}_1$ and $\mathbf{x}_2$ are also medially linked, as are $\mathbf{x}_1$ and $\mathbf{x}_3$, etc.

From this, the conditions for medial linkage can be easily derived. For example, two points $\mathbf{x}_1, \mathbf{x}_2 \in \partial S$ are medially linked if and only if there exists $R > 0$ such that

$$\mathbf{x}_1 - R\mathbf{N}_1 = \mathbf{x}_2 - R\mathbf{N}_2 \text{ and} \quad (1)$$

$$\|\mathbf{y} - (\mathbf{x}_1 - R\mathbf{N}_1)\| \geq R \text{ for all } \mathbf{y} \in \partial S. \quad (2)$$

The conditions ensure that (1) there exists a ball B with center $\mathbf{x}_1 - R\mathbf{N}_1$ and radius R that is tangent to ∂S at $\mathbf{x}_1$ and $\mathbf{x}_2$, and (2) that the ball B is contained in S. A ball satisfying these two conditions (bitangent and inscribed) is a MIB. A 2D diagram of medial axis geometry is given in Fig. 4 to conceptually illustrate these constraints. Note that although a boundary point can be linked to any number of other boundary points, Eqs. (1,2) and Fig. 4 illustrate a particular example of a boundary point $\mathbf{x}_1$ that is medially linked to only one other boundary point $\mathbf{x}_2$. Also note that the constraints in (1, 2) apply the same way in 2D and 3D.

In Section 2.2.1, the problem of fitting a medially constrained template to a target object is first formulated in the continuous case. Then in Section 2.2.2, the continuous problem is discretized and solved numerically.

2.2.1. Continuous formulation of boundary-first deformable medial modeling

—Suppose an object S is a template whose MAT has the desired branching structure, and T is a target object (Fig. 5a–b). The goal is to deform S, making it as similar as possible to T, while maintaining the branching structure of $MAT(S)$ during template deformation. Let U be a parametric domain such as the unit sphere, and $\mathbf{x} : U \to \partial S$ be a smooth bijective map that provides a global parameterization of ∂S. Let $\mathscr{L} \subset U \times U$ be the set of all parameter value pairs $(\mathbf{u}, \mathbf{v})$, such that $\mathbf{u} \neq \mathbf{v}$ and $\mathbf{x}(\mathbf{u})$ and $\mathbf{x}(\mathbf{v})$ are medially linked in S. Let D be the set of diffeomorphic transformations of $\mathbb{R}^3$. For any $\Phi \in D$, let $S_\Phi = \{\mathbf{x} \in \mathbb{R}^3 : \Phi^{-1}(\mathbf{x}) \in S\}$, let $\mathbf{x}_\Phi(\mathbf{u}) = \Phi(\mathbf{x}(\mathbf{u}))$, and let $\mathbf{N}_\Phi(\mathbf{u})$ be the unit outward normal vector to ∂S_Φ at $\mathbf{x}_\Phi(\mathbf{u})$. Let μ be some measure of dissimilarity between two objects in $\mathbb{R}^3$ (e.g., mean closest-point distance), and let ρ be some measure of irregularity of a transformation. Suppose the irregularity measure ρ is weighted by a scalar value λ. The continuous medially-constrained deformable modeling problem seeks to find a transformation $\Phi^* \in D$ that satisfies

$$\Phi^* = \operatorname{argmin}_{\Phi \in D} [\mu(S_\Phi; T) + \lambda \rho(\Phi)], \quad (3)$$

subject to the following two conditions:

$$\mathbf{x}_\Phi(\mathbf{u}) - R(\mathbf{u},\mathbf{v})\mathbf{N}_\Phi(\mathbf{u}) = \mathbf{x}_\Phi(\mathbf{v}) - R(\mathbf{u},\mathbf{v})\mathbf{N}_\Phi(\mathbf{v}) \forall (\mathbf{u},\mathbf{v}) \in \mathscr{L}, \text{ and} \quad (4)$$

$$\|\mathbf{x}_\Phi(\mathbf{w}) - [\mathbf{x}_\Phi(\mathbf{u}) - R(\mathbf{u},\mathbf{v})\mathbf{N}_\Phi(\mathbf{u})]\| \geq R(\mathbf{u},\mathbf{v}) \forall (\mathbf{u},\mathbf{v}) \in \mathscr{L}, \mathbf{w} \in U, \quad (5)$$

where $R(\mathbf{u}, \mathbf{v})$ is a bounded continuous positive real-valued function on $\mathscr{L}$. The constraints (4,5) guarantee that $\mathbf{x}_\Phi(\mathbf{u})$ and $\mathbf{x}_\Phi(\mathbf{v})$ are medially linked, and hence that Φ preserves the branching structure of $MAT(S)$ under deformation, as shown in Fig. 5c–d. Conversely, any Φ

$\in D$ that preserves the branching structure of $MAT(S)$ under deformation must satisfy (4,5). Since transformations that preserve MAT branching do exist, the minimization problem above is not in theory over-constrained and solutions can be found. In practice, however, the problem must be discretized and simplified to find solutions.

2.2.2. Discrete formulation of boundary-first deformable medial modeling—In the discrete implementation, the boundary of the deformable template is represented by a triangular mesh, i.e., a piecewise linear surface with triangular elements. This mesh is an approximation of a continuous boundary surface, and medial linkage constraints (4,5) are imposed on tuples of mesh vertices. Let N_b be the number of vertices in the mesh describing the boundary of the deforming template, and let $\mathbf{x}_i$ denote the position of each vertex $i \in [1, N_b]$. Medial links between vertices are encoded by assigning each vertex i a medial link index $M_i \in \mathbb{N}$. Any boundary mesh vertices that have the same medial link index are considered medially linked, meaning that they are members of the same MIB. For the deformable template of the aortic valve apparatus, most boundary vertices are linked to one other vertex, indicating that they belong to a MIB centered somewhere on the interior of the medial axis. Some vertices are not linked to any others since they belong to only one MIB centered along a medial edge. Some vertices are linked to two other vertices since they belong to a MIB centered on a seam curve of the medial axis.

Once a mesh conforming to the above requirements is created, the problem of deforming it to target object T is formulated as a quadratically constrained quadratic programming (QCQP) numerical optimization problem. In its most general form, this optimization problem is given as:

$$\xi^* = \operatorname{argmin}_{\xi \in \mathbb{R}^{N_v}} f(\xi; T) \text{ subject to } \alpha_c \leq g_c(\xi) \leq \beta_c \text{ for } c \in [1, N_c], \quad (6)$$

where f is the objective function being minimized, ξ is a vector of variables, and g_c are the constraint functions with bounds α_c and β_c. In this problem, there are N_v variables and N_c constraints. The objective function f and the constraint functions g_c are formulated as quadratic functions. Using quadratic functions simplifies and speeds up optimization, although it does not make the problem convex, and hence iterative techniques must be used, and no guarantees regarding finding a global, rather than local minimum, can be made. However, this is also the case for other gradient-based deformable modeling methods including m-rep and cm-rep.

In the subsections below, we specify how the objective function and the constraint functions in (6) are formulated so as to encode the problem of fitting a deformable medial model parameterized by ξ to the target object T. In short, we formulate the objective function as $f(\xi; T) = \mu(\xi; T) + \lambda \rho(\xi)$, where μ is a term measuring dissimilarity between the deformable model and the target object, and ρ is a regularization prior term with weight λ. The dissimilarity, μ, is based on the iterative closest point (ICP) algorithm (Besl and McKay, 1992), which lends itself easily to the quadratic form. The regularization penalty ρ is used to impose smoothness on the deformable model mesh and is formulated as the residual between the deforming template mesh and the best approximation of this mesh by a smooth triangular spline. The constraints specified by g_c include the discrete equivalents of the equalities and inequalities given in (4,5) that preserve medial linkages, as well as mesh quality constraints. The vector of variables ξ includes the coordinates $\mathbf{x}_i$ of the boundarty vertices in the deformable model mesh, as well as a large number of additional "helper" variables introduced in order to give all the constraints g_c a quadratic form. The terms forming the objective function, regularization prior, and the constraints are described in Sections 2.2.2.1 – 2.2.2.4, and a more detailed description of the optimization variables and constraints are given in Appendices A1 and A2, respectively. A common thread in the definitions of the terms composing functions f and g_c is the use of additional helper variables that keep f and g_c quadratic and as sparse as possible.

Section 2.2.2.1. Similarity to Target Shape: The similarity term in the objective function f is based on the ICP algorithm. At the beginning of optimization, each vertex on the template mesh is matched to the closest vertex on the target mesh, i.e., the triangular mesh representing the boundary of the target object. In our experiments, the target mesh is obtained by contour extraction from a multi-label segmentation of the target object, and has inter-vertex spacing on the order of the voxel size. Conversely, a regularly sampled subset of vertices in the target mesh is matched to the closest points (not necessarily vertices) on the template mesh. Note that the slightly asymmetric way in which the template and target points are matched is due to the difference in the sizes (number of vertices and average triangle size) of the two meshes.

The ICP objective term is equal to the sum of squared distances between all the pairs of matched points. Specifically, for each vertex $\mathbf{x}_i$ on the model boundary, let $\mathbf{y}_i$ be the target mesh vertex that is closest to $\mathbf{x}_i$ at the start of the optimization. Likewise, for a target mesh vertex $\mathbf{z}_j$, let $\mathbf{z}_j^{'}$ be the closest point on the template mesh, inside the triangle $\{\mathbf{x}_{i_{j,1}}, \mathbf{x}_{i_{j,2}}, \mathbf{x}_{i_{j,3}}\}$ and with barycentric coordinates $w_{j,1}$, $w_{j,2}$, $w_{j,3}$. The objective function is formulated as follows:

$$\mu(\xi;T)=\frac{1}{N_b}\sum_{i=1}^{N_b}\|\mathbf{x}_i-\mathbf{y}_i\|^2+\frac{1}{N_s}\sum_{j=1}^{N_s}\left\|\mathbf{z}_j-\sum_{d=1}^{3}w_{j,d}\mathbf{x}_{i_{j,d}}\right\|^2, \quad (7)$$

where N_s is the number of regularly sampled points on the target object. As in the original ICP algorithm, the matching and optimization are alternated for several iterations until convergence.

Section 2.2.2.2. Regularization: The regularization penalty $\rho(\xi)$ is formulated as the residual between the boundary of the deformable model and the best approximation of the boundary by a smooth triangular spline. Such a term propels the model to be as smooth as possible while still allowing it to satisfy the necessary medial linkage constraints. The specific implementation uses Loop subdivision surfaces (Loop, 1987), a kind of a spline with triangular elements. During the initial template generation process, discussed in Section 2.3.2 below, the template mesh is generated by applying Loop subdivision to a coarse mesh.

Specifically, let $\hat{\mathbf{X}}$ be a $N_q \times 3$ matrix of the vertices in the coarse template mesh. Then the $N_b \times 3$ matrix of the vertices in the smooth subdivided mesh can be expressed as $W\hat{\mathbf{X}}$, where W is an $N_b \times N_q$ sparse matrix of coefficients from the subdivision scheme, which only depends on the structure of the coarse mesh, and remains fixed during model deformation. As the model deforms, the regularization penalty ρ is defined as the residual distance between the vertices on the model's boundary and their best approximation by a mesh subdivided from $\hat{\mathbf{X}}$:

$$\rho(\xi)=\min_{\hat{\mathbf{X}}}\|\mathbf{X}-W\hat{\mathbf{X}}\|^2 \quad (8)$$

where $\mathbf{X}$ is a $N_b \times 3$ matrix of the vertices in the deforming model. The residual distance above could be computed for a given $\mathbf{X}$ using the method of least squares, leading to the expression $\rho(\xi) = \mathbf{X}^t W(W^t W)^{-1} W^t \mathbf{X}$. In our implementation, the vertices $\hat{\mathbf{X}}$ of the coarse mesh are instead included in the variable vector ξ as additional optimization variables. This results in $\rho(\xi)$ having the form $\|\mathbf{X} - W\hat{\mathbf{X}}\|^2$, where W is sparse. Overall, including $\hat{\mathbf{X}}$ as additional optimization variables leads to a simpler optimization problem, albeit with a slightly larger number of unknowns.

Section 2.2.2.3. Medial Linkage Constraints: Medial linkage constraints are used to ensure that any two vertices (i, j) for which $M_i = M_j$ satisfy discrete versions of the conditions of medial linkage (4) and (5). Let $k = M_i = M_j$. The first condition (4) has the form $\mathbf{x}_i - R_k\mathbf{N}_i = \mathbf{x}_j - R_k\mathbf{N}_j$, where R_k is included as an additional variable in the optimization (analogous to R in the continuous case), and $\mathbf{N}_i$ is the approximation of the unit normal vector to the boundary at $\mathbf{x}_i$. The computation of $\mathbf{N}_i$ requires taking a square root, which would make the constraint non-quadratic. Instead of computing $\mathbf{N}_i$ directly, it is treated as an additional helper variable in the optimization, and additional quadratic constraints are imposed to make $\mathbf{N}_i$ orthogonal to ∂S and unit length, as described in Appendix A2.

Note that constraints on R_k for vertices that are not medially linked to any other vertex have not yet been defined. In the continuous case, such points need not be dealt with, since MIBs that have a single point of tangency with the boundary are limit cases of MIBs with double tangency (Giblin and Kimia, 2004). In the discrete case, these vertices need to be dealt with explicitly. The radius of a singly tangent MIB is the reciprocal of the larger principal curvature of the boundary at the point of tangency. This leads to the constraint $R_{M_i} \cdot \kappa_1^i = 1$, where κ_1^i is the approximation of the larger principal curvature at $\mathbf{x}_i$. The approximation of κ_1^i is not quadratic in $\mathbf{x}_i$, but, similar to the normal vector, additional variables and constraints are introduced to the optimization problem to keep all constraints quadratic, as described in Appendix A1–2. The added variables are the elements of the first fundamental form, the elements of the shape operator, and the principal curvatures.

The medial linkage condition that mirrors (5) has the form $\|\mathbf{x}_j - (\mathbf{x}_i - R_{M_i}\mathbf{N}_i)\|^2 \geq R_{M_i}^2$ for all pairs of vertices i and j. These constraints are quadratic in the variables $\mathbf{x}_i$, $\mathbf{N}_i$, and R. However, there are $O(N_b^2)$ constraints, which does not scale well for larger meshes. Fortunately, in practice, it often suffices to relax this constraint just to the vertices j that are in the one-ring neighborhood of i. Analogous relaxation of a global non self-intersection condition is used in continuous m-reps (i.e., positive medial-boundary Jacobian condition) (Pouch et al., 2012).

Section 2.2.2.4. Mesh quality constraints: For the approximations of the unit normal and principal curvature on a triangular mesh to be accurate, the triangular elements must not be degenerate. Therefore, additional constraints are introduced on the minimal angle of each boundary triangle, and on the minimum dihedral angle between adjacent triangles. As before, additional helper variables are added into the optimization problem, such as the area of each triangle, the unit normal to each triangle, and the length of each edge, and these variables are related to one another and the vertex coordinates using quadratic constraints (Appendices A1 – A2).

Section 2.2.2.5. Numerical Solution: The optimization problem for deformable modeling with preservation of medial links involves a large number of variables ($\mathbf{x}_i$, $\mathbf{N}_i$, R_{M_i}, κ_1^i, and several others) and a large number of constraints. However, the constraints and the objective function are quadratic in the variables, i.e., have the form $f(\xi)=\xi^t A_0 \xi + b_0^t \xi$ and $g_c(\xi)=\xi^t A_c \xi + b_c^t$, where the matrices A_0 and A_c are sparse. Although these matrices are not positive definite, and thus the problem is non-convex and a global solution cannot be guaranteed, the optimization problem can be solved efficiently using interior point methods. Our implementation uses the IPOPT method (Wächter et al., 2006), and the MA97 routine in the HSL library (http://www.hsl.rl.ac.uk/) to solve sparse linear systems.

2.3. Deformable medial modeling of the aortic valve apparatus

2.3.1. Aortic valve model definitions—The aortic valve apparatus is an example of an anatomic structure with a branching medial scaffold, meaning that the medial scaffold consists of several surfaces that meet at curves, referred to as seams. As illustrated in Fig. 1, delineation of the aortic valve in this work extends from the LVO to the STJ and includes the bulbous aortic sinuses and three cusps (left, right, and non-coronary). The aortic root is modeled as a tubular shape to which three fin-like surfaces (the aortic cusps) are attached. The semilunar attachments of the cusps are seams in the medial scaffold. Free edges occur at the level of the LVO and STJ, as well as at the cusps' free margins.

Fig. 6 illustrates the 3D medial geometry of the aortic valve apparatus with the medial scaffold shown as a triangulated surface visible through a translucent gray boundary. The three aortic cusps are displayed in blue and the medial seams (the cusp attachment sites) are shown as red curves. The figure illustrates that a MIB centered at the edge of the medial axis (along the STJ, for example) is tangent to the boundary at a single point. A MIB centered on the interior of the medial axis has two points of tangency with the boundary, and a MIB centered along a seam curve has three points of tangency. In the case of the aortic valve apparatus, boundary points may be medially linked to one, two, or no other boundary points.

2.3.2. Template generation for deformable medial modeling—Deformable modeling requires a pre-defined model, or template, of the anatomic structure that is deformed to new instances of that structure in target images. Template generation need only be performed once; thereafter, the same template can be used to capture the geometry of new instances of that structure with the same medial axis branching configuration. In this work, a triangulated mesh discretely represents the continuous boundary of the aortic root and cusps. As described in Section 2.2.2, medial links are encoded on the mesh by assigning each vertex i a medial link index $M_i \in \mathbb{N}$. Any mesh vertices that share the same medial link index are considered medially linked, meaning that they are constrained to always belong to the same MIB. In addition to establishing these medial linkages, the mesh template is constructed such that each triangle on the mesh is linked to exactly one other triangle. If vertices (i, j, k) form a triangle, then there exists exactly one other triangle (i', j', k') such that $M_i = M_{i'}, M_j = M_{j'}, M_k = M_{k'}$.

The process of generating a boundary mesh of the aortic valve apparatus is illustrated in Fig. 7. It employs a user interactive tool that enables a user to first create a triangulated mesh of the aortic valve skeleton, from which a boundary mesh is then computed. The first step in this process is to obtain a manual segmentation of the valve apparatus (Fig. 7a) and compute the 3D Voronoi skeleton of that segmentation (Fig. 7b). Then the user selects points on the skeleton and tags the points as belonging to the edge, interior, or seam of the skeleton (Fig. 7c). The user triangulates these points (Fig. 7d) and associates an anatomical label to each triangle indicating whether the triangle belongs to one of the three aortic cusps, a sinus segment, or the left ventricular outflow segment (Fig. 7e). The result is a coarse mesh representation of the aortic valve's 3D medial scaffold. To obtain a boundary representation from the skeleton, a duplicate of the medial mesh is created and the two copies of the mesh are "inflated" to give the aortic root walls and cusps finite thickness [Yushkevich et al., 2013]. The inflated surface is shown in translucent gray superimposed on the skeleton in Fig. 7f. Medial link indexes are assigned to the boundary vertices based on the their relationship to the medial scaffold. For example, if two boundary nodes are inflated from the same node on the medial mesh, then those boundary nodes are assigned the same medial index. The coarse boundary mesh (Fig. 7g) is then subdivided using the Loop scheme (1987) to obtain a smooth model of the aortic valve apparatus as shown in Fig. 7h.

3. EXPERIMENTS

3.1. Image dataset

Transesophageal 3DE images of the aortic valve were acquired from 23 human subjects with normal aortic valve structure and function. One of these 23 datasets was randomly selected to create the deformable template described in Section 2.3.2, and the other 22 datasets were used in a leave-one-out cross-validation experiment to evaluate the image analysis pipeline. In addition to these normal datasets, a 3DE dataset was acquired from a single subject with one of the following diseases: Marfan syndrome, moderate aortic stenosis, and congenital bicuspid aortic valve disease. The goal of acquiring the disease datasets was to demonstrate that the pipeline can capture a range of pathological aortic valve morphologies. The images were acquired with the iE33 platform (Philips Medical Systems, Andover, MA) using a 2 to 7 MHz matrix-array transducer. For each subject, a 3DE image of the open aortic valve at mid systole was selected for analysis. The images were exported in Cartesian format with an approximate size of 224 × 208 × 208 voxels with nearly isotropic resolution of 0.4 to 0.8 mm.

3.2. Manual segmentation

Manual segmentations of the 23 3DE images of the normal aortic valve were completed. One randomly-selected segmentation was used to guide manual generation of the deformable template (Section 2.3.2) and the other 22 manual segmentations served as reference data and gold standards for the automated segmentation process (Section 3.3). Manual labeling of the 3DE images was accomplished with ITK-SNAP (Yushkevich et al., 2006b), an open-source software package for interactive medical image segmentation. A total of 5 labels were used, including one label for each of the three aortic cusps, a single label for the aortic sinuses, and a label for the left ventricular segment extending from the LVO to the cusp attachment sites. These anatomical labels are the same as those shown on the template mesh in Fig. 7.

3.3. Automated aortic valve segmentation

3DE segmentation with deformable medial modeling was performed in multiple steps: manual identification of five landmarks on the aortic valve apparatus, automatic segmentation of the aortic valve apparatus with multi-atlas joint label fusion, and boundary-first deformable medial modeling of the aortic valve in the 3DE image.

To guide model fitting to a target 3DE image, a preliminary segmentation of the aortic root was obtained by multi-atlas joint label fusion. Briefly, a collection of atlases (3DE images and labels for the aortic valve components) was registered to a target image, first with a landmark-guided affine transformation and then diffeomorphic deformable registration (Avants et al., 2008). The manually identified landmarks used for registration initialization included the three commissures of the aortic valve and points in the center of the outflow tract at the levels of the LVO and the STJ. The candidate segmentations generated by each atlas were fused to create a consensus segmentation using the weighted voting method detailed in (Wang et al., 2013). The fitting of a medially constrained parametric boundary model to the consensus segmentation was implemented as an ICP surface matching problem, as described in Section 2.2.2.1. Since ICP is sensitive to initialization, deformable registration between the template in Fig. 7 and the multi-atlas segmentation of the target image was performed to initialize the template prior to ICP surface matching. The ICP algorithm was implemented such that boundary points on the template mesh with a given anatomical label were matched to points on the target surface with the same anatomical label.

3.3 Analysis of the segmentation results

3.3.1. Evaluation of automated segmentation and deformable medial modeling —The 22 3DE images of the normal aortic valve that were not used for deformable template generation were automatically segmented in a leave-one-out cross-validation experiment. Each of the 22 3DE images was treated as a target image for segmentation, and the other 21 images and their manual segmentations were used as reference atlases for multi-atlas label fusion. The deformable medial model was fitted to the segmentation of the target image obtained by multi-atlas label fusion and compared to the manual segmentation of the target image. In addition, to evaluate the relative contributions of each step of the segmentation process, the manual segmentation of the target image was also compared to the mutli-atlas segmentation without model fitting and to the result of fitting a deformable medial model directly to the manual segmentation. The metric used to compare these segmentations was the symmetric mean boundary error (MBE). Given two meshed shapes *P* and *Q*, the MBE is defined as follows:

$$MBE=\frac{1}{2}(d(P,Q)+d(Q,P)), \quad (9)$$

where $d(P, Q)$ is the distance from *P* to *Q* and $d(Q, P)$ is the distance from *Q* to *P*. The distance between two meshes is given by

$$d(P,Q) \cong \frac{1}{A_p}\int_{x\in P}\inf_{y\in Q}\|x-y\|dA \quad (10)$$

where *x* is a point on mesh *P*, *y* is a point on mesh *Q*, and A_P is the surface area of mesh *P*.

3.3.2. Comparison of morphological measurements derived from manual and automated segmentation—The morphological measurements listed below were automatically computed from the deformable model fitted to the results of multi-atlas segmentation. 3D contours of the STJ, aortic annulus (basal leaflet attachments), the cusp tips, and the LVO were automatically identified on the deformable model. Points on the STJ were identified as boundary nodes associated with the medial edge of the sinus segment, and points on the LVO were identified as boundary nodes associated with the medial edge of the left ventricular outflow segment. The seams of the medial mesh demarcated the crown-shaped aortic annulus, and the free edges of the cusps were identified as the cusp tips. Each aortic valve model was centered at the origin of the Cartesian coordinate system and rotated to maximize the sum of areas enclosed by projections of the STJ, the leaflet tips, and the LVO onto the x-y plane. For comparison, the same measurements computed from the automated segmentation (i.e., the template fitted to the results of multi-atlas label fusion) were also computed from the deformable model fitted directly to the manual segmentation.

- Mean STJ diameter (STJD): mean diameter of the STJ contour projected onto the x-y plane
- STJ area (STJA): area enclosed by the projection of the STJ contour onto the x-y plane
- Mean aortic sinus diameter (ASD): mean diameter of the contour that encloses the projection of the aortic sinuses onto the x-y plane
- Aortic sinus area (ASA): area enclosed by the projection of the aortic sinuses onto the x-y plane
- Valve orifice area (VOA): area enclosed by the projection of the cusp tips onto the x-y plane
- Mean aortic annulus diameter (AAD): mean diameter of the projection of the contour defining the cusp attachments onto the x-y plane

- Aortic annulus area (AAA): area enclosed by the projection of the leaflet basal attachments onto the x-y plane
- Surface area of each aortic cusp (SALC, SANC, SARC): mean of the aortic and ventricular surface areas of each cusp
- Mean leaflet thickness (TLC, TNC, TRC): mean thickness of each cusp, defined as the average distance between boundary nodes with the same medial index

3.3.3. Segmentation and deformable medial modeling of pathological aortic valve morphology—To demonstrate that boundary-first deformable medial modeling can capture diseased aortic valve morphologies in addition to normal aortic valve geometry, multi-atlas segmentation and model fitting were performed on image data acquired from a subject with Marfan syndrome and a subject with moderate aortic stenosis. Multi-atlas segmentation was performed using 22 normal 3DE aortic valve atlases as references. In addition to capturing these two disease states, the boundary-first deformable medial modeling method was tested on an example of a bicuspid aortic valve, a congenital abnormality in which the aortic valve has two leaflets rather than three. In this particular subject, the left and right coronary cusps were fused into a single cusp. Since bicuspid atlases were not available for automated bicuspid valve segmentation, a template of a bicuspid valve was generated from and fitted to a manual segmentation to demonstrate the potential extension of boundary-first medial modeling to bicuspid aortic valve morphometry. The same clinically relevant measurements described above were computed from the fitted deformable model of each disease case.

4. Results

The template mesh fitted to the multi-atlas segmentations had 476 vertices and 952 triangles. The corresponding constrained optimization problem had 12296 variables (88% of the variables were helper variables used to make the problem quadratic), 11308 equality constraints and 4320 inequality constraints. The Jacobian of the constraints was 99.94% sparse, and the Hessian of the Lagrangian was 99.93% sparse. Constrained optimization was successful in all subjects, converging to a local minimum of f and satisfying all the constraints within the tolerance of 10^{-8}. Each ICP iteration required on the order of 50 optimization steps to converge, taking an average of 1.5 minutes on a single 2.4GHz Intel CPU core. The number of ICP iterations was fixed at 10 for each subject. The bulk of the computation time was devoted to solving sparse linear problems involving the Lagrangian and Jacobian matrices.

A representative result of segmentation with boundary-first deformable medial modeling is presented in Fig. 8. The deformable medial model (fitted to the result of multi-atlas segmentation), the multi-atlas segmentation, and manual segmentation are displayed in two different orientations. The fitted model is shown superimposed on the grayscale 3DE image.

The mean boundary errors between the automated and manual segmentations are presented in Table 1. The first row measures the accuracy of the combined multi-atlas segmentation and deformable medial modeling relative to expert manual segmentation, and thus is the primary performance metric for our method. The second row gives the accuracy for multi-atlas segmentation without deformable medial modeling. The fact that these two measures are so similar indicates that the benefits of medial modeling (parametric representation, thickness mapping, etc.) can be leveraged without incurring additional costs in accuracy. Rows 3 and 4 measure the residual error for deformable medial modeling, i.e. the difference between the medial model and the target object to which it is fitted. Row 3 reports this for models fitted to manual segmentations and row 4 for models fitted to automatic multi-atlas segmentations. These differences are due to the fact that the mathematical skeleton of the segmentations is actually very complex (with hundreds or thousands of small branches) and the approximation with a three-branch medial model necessarily results in some small residual errors. Row 5 reports the mean boundary error between the deformable models fitted to the manual and multi-atlas segmentations. The 95th percentile boundary error is the maximum distance between 95% of the points on the model and manual segmentation.

Clinically relevant measurements of normal tricuspid aortic valve morphology are presented in Table 2. Similar to our earlier work evaluating clinical measurements derived from mitral valve segmentations (Pouch et al., 2012), the measurements we compare are those that were computed from the deformable model fitted to the results of multi-atlas segmentation (second column) and from the deformable model fitted directly to the manual segmentation (third column). We compare model-derived measurements (rather than measurements derived directly from the manual and multi-atlas segmentations themselves) since these measurements cannot be extracted from the manual and multi-atlas segmentations alone. Without model fitting, the manual and multi-atlas segmentations consist only of voxel labels rather than landmarks.

The segmentation results for the tricuspid aortic valves with Marfan disease and aortic stenosis are shown in the two left columns of Fig. 9. A model of the bicuspid aortic valve fitted directly to a manual 3DE segmentation is displayed in the right column of Fig. 9. Similar to normal aortic valve morphometry presented in Table 2, morphological measurements of the diseased aortic valves were computed and are presented in Table 3. The $^{(++)}$ and $^{(--)}$ symbols indicate that the measurement is greater than or less than the mean normal measurement by at least two standard deviations.

5. Discussion

The aortic valve apparatus is a geometrically complex anatomical structure that is challenging to segment in 3DE images, especially when the segmentation goal is to represent the valve volumetrically. This study demonstrates that a medially constrained boundary-first deformable medial modeling paradigm effectively accomplishes this task. A benefit of this paradigm is that it represents a structure with a branching medial topology not in an ad hoc manner, but in a way that adheres to Blum's original definition of the medial axis (1967). By preserving the branching configuration of the medial axis during model deformation, the method produces detailed patient-specific anatomical shape representations that have inter-subject point correspondences and can be statistically compared and morphometrically analyzed in a straightforward manner. In a broader context, the method extends the utility of medial modeling for medical image and statistical shape analysis since many anatomical structures have complicated geometries that cannot be represented in terms of non-branching morphological skeletons.

As a first step towards assessing the ability of boundary-first deformable medial modeling to capture varying geometries of the normal aortic valve, the template generated in Fig. 7 was fitted directly to 22 manual segmentations (excluding the manual segmentation from which the template was generated) and the symmetric MBE was computed. The result (0.23 ± 0.08 mm) demonstrates that the medial model can accurately represent normal variations in shape of the entire aortic valve apparatus. To assess the quality of automated segmentation with deformable medial modeling, the MBE between the manual segmentations and the medial models fitted to the results of multi-atlas segmentation was computed (0.41 ± 0.10 mm) and was on the order of one voxel. The similarity between the automated and manual segmentation and the ability of the automatically generated model to capture valve morphology in the 3DE grayscale image can be qualitatively appreciated in Fig. 8. The MBE between the manual and multi-atlas segmentations *without* model fitting (0.32 ± 0.13 mm) was similar to the result obtained *with* model fitting, suggesting that improvements in multi-atlas segmentation could enhance the accuracy of model fitting. The manual versus automatic segmentation comparison in this study is on par with one of few studies on automatic aortic valve segmentation in 3DE images, wherein Ionasec et al. report an MBE of 1.54 ± 1.17 mm (2010). Notably, our work is the first to achieve *volumetric* segmentation of the valve with a high level of accuracy (MBE on the order of one voxel). The importance of representing the aortic valve apparatus as a structure with locally varying thickness is that thickness is a meaningful tissue parameter in biomechanical analysis and simulation of the valve. It can also be a marker of valve pathology, such as calcification or thinning of the aortic valve components.

The results of this study highlight the benefits of combining multi-atlas segmentation with deformable medial modeling, techniques that have been applied to a range of image analysis applications. While multi-atlas segmentation assigns labels to voxels in the 3D image data, deformable medial modeling takes the next step of identifying landmarks and facilitating statistical comparison of skeleton-derived shape features such as thickness. For this reason, it is not possible to reliably extract the morphological measurements presented in Tables 2 and 3 from the multi-atlas segmentation alone. Moreover, no global shape constraints are used to guarantee the topology of the multi-atlas segmentation, which is another advantage of integrating multi-atlas segmentation with a deformable modeling scheme that ensures a consistent medial axis branching configuration on image-derived models of the aortic valve apparatus. While other 3D model fitting techniques in the literature, such as topology-preserving level sets (Han et al., 2003, Hsu et al., 2008, Ségonne, 2008), also impose topology constraints on image segmentation results, the constraints do not prescribe an immutable medial axis branching configuration on the segmentation, which would make it difficult to compare skeleton-derived features of valves of different subjects. In terms of image segmentation methods that use volumetric models that preserve medial axis topology, deformable modeling with the finite element method (FEM) (Bro-Nielsen et al., 1996, Park et al., 1996, Pham et al., 2001) are similar to the work presented here. To the best of our knowledge, however, FEM-based methods have not explicitly described the extraction of skeleton-derived shape features.

While the symmetric MBE metric is a useful way of evaluating the accuracy of shape representation and segmentation accuracy, it is also important to assess the similarity in clinical measurements derived from manual and automated valve segmentations. Since the deformable medial model captured the shape of the manual and multi-atlas segmentations with minimal error (MBE of 0.23 ± 0.08 mm and 0.22 ± 0.04 mm, respectively) and the clinical measurements could not be computed directly from the manual and multi-atlas segmentations themselves, the “manual” and “automated” measurements in Table 2 were derived from deformable medial models fitted directly to the manual and multi-atlas segmentation results. The comparison of these measurements in Table 2 demonstrates good to excellent correlation with minimal bias between measurements derived from the automated and manual segmentations.

Segmentation with boundary-first deformable medial modeling is not only able to represent normal tricuspid aortic valve geometry; this work demonstrates that the method can delineate pathological valve morphologies, even with the use of “normal” reference atlases for multi-atlas label fusion. Pathological features, such as thickening of the right coronary cusp and sinus segments in the stenotic aortic valve (Fig. 9, first column) and marked enlargement of the aortic valve and thinning of the non-coronary cusp in the patient with Marfan disease (Fig. 9, second column) are patient-specific abnormalities that are both qualitatively and quantitatively captured with 3DE image analysis. The morphological measurements presented in Table 3 indicate that pathological variations in valve morphology (greater than or less than two standard deviations from controls) can be quantitatively identified. Although reference atlases for bicuspid aortic valves are not currently available, the ability of the presented method to model and quantitatively analyze bicuspid aortic valve morphology is shown. The bicuspid aortic valve is an example of a pathology that requires a different atlas set and deformable template than normal and diseased tricuspid aortic valves since bicuspid valves have a different topology and medial axis branching configuration than tricuspid aortic valves.

Limitations of the current work include segmentation of the aortic valve at a single phase in the cardiac cycle (rather than at multiple time points in the real-time 3DE series) and the requirement for manual initialization of multi-atlas label fusion. These limitations will be the focus of future research, but do not diminish the importance of the methodology and results presented in this work. Segmentation at multiple time points in the cardiac cycle would require one-time generation of reference atlases of the aortic valve in the diastolic phase. Since multi-atlas segmentation and deformable medial modeling have effectively captured mitral valve morphology in 3DE images acquired at multiple phases in the cardiac cycle (Pouch et al., 2014), it is reasonably expected that the methods presented here will likewise be applicable to segmentation of the aortic valve in a complete real-time 3DE image series. The efficacy of feature-based automatic landmark detection techniques, such as the scale-invariant feature transform (Lowe, 2004), potentiates a future automatic landmark-based initialization of multi-atlas segmentation. A third limitation of this study is the possibility of shape approximation bias introduced by the construction of the deformable medial template from a single subject's dataset. We estimated this bias by computing how accurately the template captured the shape of the manual segmentation from which it was generated. The mean boundary error was 0.22 mm, which is very close to the mean boundary error of the template fitted directly to all the other manual segmentations (Table 1, third row). This result suggests minimal shape approximation bias since the template did not capture its manual segmentation dramatically better than the other 22 segmentations. Nevertheless, future work could employ a strategy for unbiased template estimation. One way to accomplish this is to fit a biased template to all subjects, compute an average and use the result as the new template. This process could be performed iteratively.

Several previous studies of 3D aortic valve morphology involve planimetric measurements derived from multidetector computed tomography (MDCT) image data (Akhtar et al., 2009, Messika-Zeitoun et al., 2010). While there are a number of benefits to MDCT imaging, such as easy identification of the coronary ostia, 3DE has a higher temporal resolution and does not require the administration of contrast agents or ionizing radiation. For this reason, model-based analysis of 3DE images can provide complementary information to MDCT planimetry that facilitates enhanced aortic valve diagnostics, interactive visualization and quantitative assessment of patient-specific aortic valve morphologies, and the development of novel devices and approaches to surgical treatment for aortic valve disease.

Acknowledgments

This work was supported by the National Institutes of Health: HL119010, HL103723, EB017255, EB014346, and NS045839.

References

Akhtar M, Tuzcu EM, Kapadia SR, Svensson LG, Greenberg RK, Roselli EE, Halliburton S, Kurra V, Schoenhagen P, Sola S. Aortic root morphology in patients undergoing percutaneous aortic valve replacement: Evidence of aortic root remodeling. Journal of Thoracic Cardiovascular Surgery. 2009; 137(4):950–6. [PubMed: 19327523]

Avants BB, Epstein CL, Grossman M, Gee JC. Symmetric diffeomorphic image registration with cross-correlation: evaluating automated labeling of elderly and neurodegenerative brain. Med Image Anal. 2008; 12:26–41. [PubMed: 17659998]

Besl PJ, McKay ND. A method for registration of 3D shapes. IEEE Transactions on Pattern Analysis and Machine Intelligence. 1992; 14(2):239–256.

Bouix S, Pruessner JC, Collins DL, Siddiqi K. Hippocampal shape analysis using medial surfaces. Neuroimage. 2005; 25(4):1077–89. [PubMed: 15850726]

Blum, H. A transformation for extracting new descriptors of shape. In: Wathen-Dunn, W., editor. Models for the Perception of Speech and Visual Form. MIT Press; Cambridge: 1967. p. 362-380.

Bro-Nielsen M, Cotin S. Real-time volumetric deformable models for surgery simulation using finite elements and condensation. Computer Graphis Forum. 1996:57–66.

Giblin P, Kimia BB. A formal classification of 3D medial axis points and their local geometry. IEEE Transactions on Pattern Analysis and Machine Intelligence. 2004; 26(2):238–251. [PubMed: 15376898]

Han X, Xu C, Prince JL. A topology preserving level set method for geometric deformable models. IEEE Transactions on Pattern Analysis and Machine Intelligence. 2003; 25(6):755–768.

Hsu C, Yang C, Wang H. Topological control of level set method depending on topology constraints. Pattern Recognition Letters. 2008; 29(4):537–546.

Ionasec RI, Voigt I, Georgescu B, Wang Y, Houle H, Vega-Higuera F, Navab N, Comaniciu D. Patient-specific modeling and quantification of the aortic and mitral valves from 4-D cardiac CT and TEE. IEEE Trans Med Imaging. 2010; 29:1636–1651. [PubMed: 20442044]

Jassar AS, Levack MM, Solorzano RD, Pouch AM, Ferrari G, Cheung AT, Ferrari VA, Gorman JH III, Gorman RC, Jackson BM. Feasibility of in vivo human aortic valve modeling using real-time three-dimensional echocardiography. Ann Thorac Surg. 2014; 97:1255–9. [PubMed: 24518577]

Loop, C. Master's thesis. Department of Mathematics, University of Utah; 1987. Smooth subdivision surfaces based on triangles.

Lowe DG. Distinctive image features from scale-invariant keypoints. International Journal of Computer Vision. 2004; 60(2):91–110.

Messika-Zeitoun D, Serfaty JM, Brochet E, Ducrocq G, Lepage L, Detaint D, Hyafil F, Himbert D, Pasi N, Laissy JP, Iung B, Vahanian A. Multimodel assessment of the aortic annulus diameter: Implications for transcatheter aortic valve implantation. Journal of the American College of Cardiology. 2010; 55(3):186–94. [PubMed: 20117398]

Noack T, Kiefer P, Ionasec R, Voigt I, Mansi T, Vollroth M, Hoebartner M, Misfeld M, Mohr FW, Seeburger J. New concepts for mitral valve imaging. Ann Cardiothorac Surg. 2013; 2(6):787–95. [PubMed: 24349983]

Park J, Metaxas D, Axel L. Analysis of left ventricular wall motion based on volumetric deformable models and MRI-SPAMM. Medical Image Analysis. 1996; 1(1):53–71. [PubMed: 9873921]

Pham, QC.; Vincent, F.; Clarysse, P.; Croisille, P.; Magnin, IE. A FEM-based deformable model for the 3D segmentation and tracking of the heart in cardiac MRI. Proceedings of the 2nd International Symposium on Image and Signal Processing and Analysis; 2001. p. 250-254.

Pizer SM, Fritsch DS, Yushkevich PA, Johnson VE, Chaney EL. Segmentation, registration, and measurement of shape variation via image object shape. IEEE Trans Med Imaging. 1999; 18(1): 851–865. [PubMed: 10628945]

Pizer SM, Fletcher PT, Joshi S, Thall A, Chen JZ, Fridman Y, Fritsch DS, Gash AG, Glotzer JM, Jiroutek MR, Lu C, Muller KE, Tracton G, Yushkevich P, Chaney EL. Deformable m-reps for 3D medical image segmentation. International Journal of Computer Vision. 2003; 55:85–106. [PubMed: 23825898]

Pizer, SM.; Jung, S.; Goswami, D.; Vicory, J.; Zhao, X.; Chaudhuri, R.; Damon, JN.; Huckemann, S.; Marron, JS. Nested sphere statistics of skeleton models. In: Breuss, M.; Bruckstein, A.; Maragos, P., editors. Innovations for Shape Analysis Mathematics and Visualization. Springer; Berlin Heidelberg: 2013. p. 93-115.

Pouch AM, Yushkevich PA, Jackson BM, Jassar AS, Vergnat M, Gorman JH III, Gorman RC, Sehgal CM. Development of a semi-automated method for mitral valve modeling with medial axis representation using 3D ultrasound. Medical Physics. 2012; 39(2):933–950. [PubMed: 22320803]

Pouch, AM.; Wang, H.; Takabe, M.; Jackson, BM.; Sehgal, CM.; Gorman, JH., 3rd; Gorman, RC.; Yushkevich, PA. Automated segmentation and geometrical modeling of the tricuspid aortic valve in 3D echocardiographic images. In: Mori, K.; Sakuma, I.; Sato, Y.; Barillot, C.; Navab, N., editors. MICCAI 2013, LNCS. Vol. 8149. Springer; Berlin Heidelberg: 2013. p. 485-492.

Pouch AM, Wang H, Takabe M, Jackson BM, Gorman JH 3rd, Gorman RC, Yushkevich PA, Sehgal CM. Fully automatic segmentation of the mitral leaflets using multi-atlas label fusion and deformable medial modeling. Med Image Anal. 2014; 18(1):118–129. [PubMed: 24184435]

Pouch, AM.; Tian, S.; Takabe, M.; Wang, H.; Yuan, J.; Cheung, AT.; Jackson, BM.; Gorman, JH., III; Gorman, RC.; Yushkevich, PA. In: Camara, O.; Mansi, T.; Pop, M.; Rhode, K.; Sermesant, S.; Young, A., editors. Segmentation of the aortic valve apparatus in 3D echocardiographic images: Deformable modeling of a branching medial structure; Proceedings of the 5th international STACOM workshop; Boston. September 18, 2014; Berlin Heidelberg: Springer; 2015. LNCS 8896

Rausch MK, Famaey N, Shultz TO, Bothe W, Miller DC, Kuhl E. Mechanics of the Mitral Valve: A Critical Review, An In Vivo Parameter Identification, and the Effect of Prestrain. Biomech Model Mechanobiol. 2013; 12(5):1053–1071. [PubMed: 23263365]

Schneider RJ, Tenenholtz NA, Perrin DP, Marx GR, del Nido PJ, Howe RD. Patient-specific mitral leaflet segmentation from 4D ultrasound. Med Image Comput Comput Assist Interv. 2011; 14:520–527. [PubMed: 22003739]

Ségonne F. Active Contours Under Topology Control – Genus Preserving Level Sets. International Journal of Computer Vision. 2008; 79(2):107–117.

Styner M, Gerig G, Lieberman J, Jones D, Weinberger D. Statistical shape analysis of neuroanatomical structures based on medial models. Med Image Anal. 2003; 7(3):207–20. [PubMed: 12946464]

Sun, H.; Avants, BB.; Frangi, AF.; Sukno, F.; Gee, JC.; Yushkevich, PA. Cardiac medial modeling and time-course heart wall thickness analysis. In: Metaxas, D.; Axel, L.; Fichtinger, G.; Székely, G., editors. MICCAI 2008, Part II. LNCS. Vol. 5242. Springer; Heidelberg: 2010. p. 766-773.

Terriberry, TB.; Gerig, G. In: Penned, X.; Joshi, S., editors. A continuous 3-D medial shape model with branching; MICCAI 2006 Workshop on Mathematical Foundations of Computational Anatomy; 2006.

Vergnat M, Jassar AS, Jackson BM, Ryan LP, Eperjesi TJ, Pouch AM, Weiss SJ, Cheung AT, Acker MA, Gorman JH III, Gorman RC. Ischemic mitral regurgitation: A quantitative three-dimensional echocardiographic analysis. Ann Thorac Surg. 2011; 91:157–64. [PubMed: 21172506]

Veronesi F, Corsi C, Sugeng L, Mor-Avi V, Caiani EG, Weinert L, Lamberti C, Lang RM. A study of functional anatomy of aortic-mitral valve coupling using 3D matrix transesophageal echocardiography. Circ Cardiovasc Imaging. 2009; 2:24–31. [PubMed: 19808561]

Wächter A, Biegler LT. On the Implementation of an Interior-Point Filter Line-Search Algorithm for Large-Scale Nonlinear Programming. Mathematical Programming. 2006; 106:25–57.

Wang HZ, Suh JW, Das SR, Pluta JB, Craige C, Yushkevich PA. Multi-Atlas Segmentation with Joint Label Fusion. IEEE Transactions on Pattern Analysis and Machine Intelligence. 2013; 35:611–623. [PubMed: 22732662]

Yushkevich PA, Zhang H, Gee JC. Continuous medial representation for anatomical structures. IEEE Trans Med Imaging. 2006a; 25:1547–1564. [PubMed: 17167991]

Yushkevich PA, Piven J, Hazlett HC, Smith RG, Ho S, Gee JC, Gerig G. User-guided 3D active contour segmentation of anatomical structures: significantly improved efficiency and reliability. Neuroimage. 2006b; 31:1116–1128. [PubMed: 16545965]

Yushkevich PA, Zhang H, Simon TJ, Gee JC. Structure-specific statistical mapping of white matter tracts. NeuroImage. 2008; 41:448–461. [PubMed: 18407524]

Yushkevich, PA.; Zhang, HG. Deformable modeling using a 3D boundary representation with quadratic constraints on the branching structure of the Blum skeleton. In: Gee, JC.; Joshi, S.; Pohl, KM.; Wells, WM.; Zöllei, L., editors. IPMI 2013, LNCS. Vol. 7917. Springer; Berlin Heidelberg: 2013. p. 280-291.

APPENDIX

Appendix 1. Variables in the deformable modeling optimization problem

The variables that are optimized in the model fitting objective function (Eq. 6) are given by

$$\xi=\{\mathbf{x},\mathbf{m},R,\mathbf{N},\mathbf{X}_{u_{1,2}},\mathbf{N}_{u_{1,2}},\mathbf{FF1},\mathbf{SO},\kappa_1,TA,\mathbf{N}_T,E_{qr},\hat{\mathbf{x}},\csc(\alpha)\}.$$

These variables include the medially linked boundary vertices **x** that define the deformable model, as well as a number of additional helper variables that are introduced to ensure that the optimization constraints are quadratic. Each variable is defined in Table A1.I.

Table A1.I

Variables in the deformable modeling optimization problem and their descriptions.

Variable	Description
$\mathbf{x}_i$	coordinates of the boundary vertex $i \in [1, N_b]$, where N_b is the total number of vertices on the boundary mesh
$\mathbf{m}_i$	position of the medial vertex $i \in [1, N_m]$, where N_m is the total number of vertices on the medial mesh
R_i	radius of the maximally inscribed ball centered at the medial vertex $i \in [1, N_m]$, i.e. the distance from medial vertex i to the boundary
$\mathbf{N}_i$	normal vector to the boundary mesh at vertex $i \in [1, N_b]$
$\mathbf{X}^i_{u_{1,2}}=\{\mathbf{X}^i_{u_1}, \mathbf{X}^i_{u_2}\}$	pair of non-parallel vectors in the tangent plane to the boundary mesh at $\mathbf{x}_i$
$\mathbf{N}^i_{u_{1,2}}=\{\mathbf{N}^i_{u_1}, \mathbf{N}^i_{u_2}\}$	partial derivatives of the boundary normal at $\mathbf{x}_i$ at with respect to $\mathbf{X}^i_{u_{1,2}}$
$\mathbf{FF1}^i$	first fundamental form defined at boundary vertex i, which is one of N_e edge vertices on the medial mesh
$\mathbf{SO}^i$	shape operator defined at boundary vertex i, which is one of N_e edge vertices on the medial mesh
κ^i_1	larger principal curvature of the boundary patch associated with medial vertex i that is one of N_e edge vertices on the medial mesh
TA_i	area of the boundary triangle $i \in [1, N_t]$, where N_t is the total number of boundary triangles
$\mathbf{N}^i_T$	normal vector to the boundary triangle $i \in [1, N_t]$
E^i_{qr}	edge length between vertices q and r on the boundary triangle $i \in [1, N_t]$
$\mathbf{x}_{\hat{j}}$	coordinates of the vertex $j \in [1, N_q]$ of a "parent" mesh from which the vertex coordinates $\mathbf{x}_i$ were obtained via subdivision, where N_q is the total number of vertices on the coarse parent mesh
$\csc(\alpha^i_p)$	cosecant of α^i_p, which is one of three angles of boundary triangle i, where $p = \{0,1,2\}$ is the index of the triangle angle

Appendix 2. Constraints in the deformable modeling optimization problem

The equality and inequality constraints in the deformable modeling optimization problem include the medial linkage constraints described in Eqs. 4 – 5, as well as constraints that define relationships between helper variables, which are introduced to ensure that all constraints are quadratic. The constraints are divided into to four categories: constraints used to obtain differential geometric properties of the boundary (the tangent plane, boundary normals, and curvature), medial linkage constraints, constraints on the radius function at medial edges, and mesh quality constraints. Each set of constraints is described below.

Constraints used to obtain differential geometric properties of the model boundary

The tangent plane is defined at each boundary vertex i by a pair of non-parallel vectors $\mathbf{X}^i_{u_1}$ and $\mathbf{X}^i_{u_2}$ that are approximately tangent to the model's surface at the vertex i. Loop (1987) proposed to approximate such tangent vectors at a vertex on a triangular mesh as a weighted sum of the neighboring vertices. Here, Loop's tangent vector formula is given by a set of equality constraints:

$$\mathbf{X}_{u_d}^i=\sum_{k=1}^{K_i} w_k^{K_i,d}\mathbf{x}_{j_k}+w_0^{K_i,d}\mathbf{x}_i. \quad \text{A2.1}$$

K_i is the valence of boundary vertex i, j_k is the k-th neighbor of boundary vertex i, and $d \in \{1,2\}$.

The unit boundary normals $\mathbf{N}_i$ are defined by imposing three constraints that ensure that the normal is orthogonal to the tangent plane at i and that the length of $\mathbf{N}_i$ is unity.

$$\mathbf{N}_i^t\mathbf{N}_i=1; \quad \mathbf{N}_i^t\mathbf{X}_{u_1}^i=0; \quad \mathbf{N}_i^t\mathbf{X}_{u_2}^i=0, \quad \text{A2.2}$$

where $\mathbf{N}_i^t$ denotes the transpose of the normal vector $\mathbf{N}_i$.

The partial derivatives of the normal vectors with respect to directions $\mathbf{X}_{u_d}^i$ on the tangent plane are constrained based on the Loop (1987) formulas, similar to A2.1:

$$\mathbf{N}_{u_d}^i=\sum_{k=1}^{K_i} w_k^{K_i,d}\mathbf{N}_{j_k}+w_0^{K_i,d}\mathbf{N}_i \quad \text{A2.3}$$

The first fundamental form and shape operator are given by the following equality constraints, which are defined at boundary vertices i associated with edges of the medial mesh:

$$\mathbf{FF1}^i[q,r]=\mathbf{X}_{u_q}^i\mathbf{X}_{u_r}^i, \text{ where } q,r \in \{1,2\} \quad \text{A2.4}$$

$$\mathbf{FF1}^i \cdot \mathbf{SO}^i=-\begin{bmatrix} \mathbf{X}_{u_1}^i \cdot \mathbf{N}_{u_1}^i & \mathbf{X}_{u_1}^i \cdot \mathbf{N}_{u_2}^i \\ \mathbf{X}_{u_2}^i \cdot \mathbf{N}_{u_1}^i & \mathbf{X}_{u_2}^i \cdot \mathbf{N}_{u_2}^i \end{bmatrix} \quad \text{A2.5}$$

The boundary curvature is then written in terms of the shape operator:

$$(\mathrm{SO}_{11}^i-\kappa_1^i)(\mathrm{SO}_{22}^i-\kappa_1^i)=\mathrm{SO}_{21}^i \cdot \mathrm{SO}_{12}^i \quad \text{A2.6}$$

$$\kappa_1^i>\frac{1}{2}(\mathrm{SO}_{11}^i+\mathrm{SO}_{22}^i) \quad \text{A2.7}$$

Eq. A2.6 is obtained by substituting for κ_2 in the equations that define the mean and Gaussian curvatures in terms of principal curvatures: trace($\mathbf{SO}$) = $\kappa_1 + \kappa_2$ and det($\mathbf{SO}$) = $\kappa_1 \cdot \kappa_2$. Eq. A2.7 ensures that κ_1 is the larger of the two principal curvatures κ_1 and κ_2.

Medial linkage constraints

During model deformation, these constraints maintain medial linkages of boundary vertices, which ensure that the branching configuration and topology of the medial axis does not change during model fitting. The constraints are equivalent to Eq. 4 – 5 but in practice include the medial vertex $\mathbf{m}_{M_i}$ as a variable:

$$\mathbf{x}_i - (\mathbf{m}_{M_i} + R_{M_i} \mathbf{N}_i) = 0 \quad \text{A2.8}$$

$$\| \mathbf{x}_{j_k} - \mathbf{m}_{M_i} \|^2 > R_{M_i}^2 \quad \text{A2.9}$$

Here, $M_i \in [1, N_m]$ is the index of the medial vertex associated with the boundary vertex $i \in [1, N_b]$, and j_k is the k-th neighbor of vertex i. The radius is constrained as follows:

$$R_{M_i} > R_{min}. \quad \text{A2.10}$$

Here, R_{min} = 0.01 mm is chosen to be a reasonable lower limit for the radius function.

Constraints on the radius at medial edges

The radius R along the edges of the medial mesh is defined in terms of the larger principal curvature of the boundary mesh, κ_1:

$$R_i \cdot \kappa_1^i = 1 \quad \text{A2.11}$$

Since A2.11 applies only to medial edges, the constraints that are used to define boundary curvature (Eqs. A2.4 – A2.7) need not be computed at all boundary mesh vertices, but only at boundary vertices i that are associated with edges of the medial mesh.

Mesh quality constraints

The first mesh quality constraint (Eq. A2.17) prevents triangle irregularity by specifying a minimum value for the three angles of each boundary triangle. First, the triangle area and triangle normal are defined by the following equality constraints:

$$2 \cdot TA_i \cdot \mathbf{N}_T^i = (\mathbf{x}_2 - \mathbf{x}_1) \times (\mathbf{x}_3 - \mathbf{x}_1) \quad \text{A2.12}$$

$$\mathbf{N}_T^i \cdot \mathbf{N}_T^i = 1 \quad \text{A2.13}$$

Eq. A2.12 arises from $\mathbf{N}_T^i = \frac{(\mathbf{x}_2 - \mathbf{x}_1) \times (\mathbf{x}_3 - \mathbf{x}_1)}{|(\mathbf{x}_2 - \mathbf{x}_1) \times (\mathbf{x}_3 - \mathbf{x}_1)|}$ and $TA_i = \frac{|(\mathbf{x}_2 - \mathbf{x}_1) \times (\mathbf{x}_3 - \mathbf{x}_1)|}{2}$, where $\{\mathbf{x}_1, \mathbf{x}_2, \mathbf{x}_3\}$ are vertices of the boundary triangle i. Next, the edge length of each boundary triangle is defined and constrained to be positive:

$$EL_{q,r}^{i}{}^{2}=(\mathbf{x}_q-\mathbf{x}_r)\cdot(\mathbf{x}_q-\mathbf{x}_r) \quad \text{A2.14}$$

$$EL_{q,r}^{i}>0 \quad \text{A2.15}$$

Here, $\mathbf{x}_q$ and $\mathbf{x}_r$ are vertices on boundary triangle *i*. Finally, the constraint on each boundary triangle angle is specified:

$$2\cdot TA_i\cdot \csc(\alpha_p^i)=EL_{\eta_{p\oplus 0},\eta_{p\oplus 1}}^{i}\cdot EL_{\eta_{p\oplus 0},\eta_{p\oplus 2}}^{i} \quad \text{A2.16}$$

$$\csc(\alpha_p^i)>\lambda \quad \text{A2.17}$$

Eq. A2.16 defines the angle α_p^i in terms of the area and lengths of two edges of the boundary triangle *i*. The three triangle vertices are denoted by $p = \{0,1,2\}$, and $\eta_{p\oplus 1}$ is the index of the boundary node that corresponds to the triangle vertex indexed as 3 mod (p + 1). In Eq. A2.17, $\csc(\alpha_p^i)$ is constrained to be larger than λ = csc(12°) to minimize triangle irregularity on the boundary mesh.

The second mesh quality constraint enforces a minimum dihedral angle between boundary mesh triangles that share an edge:

$$\mathrm{N}_T^{q,r}\cdot \mathrm{N}_T^{r,q}>\begin{cases} \rho_b\, if\; q,r\; is\; a\; boundary\; edge \\ \rho_i\; if\; q,r\; is\; not\; a\; boundary\; edge \end{cases} \quad \text{A2.18}$$

$\mathrm{N}_T^{q,r}$ and $\mathrm{N}_T^{r,q}$ are the normals of adjacent boundary triangles that share the edge between vertices $\mathbf{x}_q$ and $\mathbf{x}_r$. In this application ρ_b = cos(26°) = −0.9 and ρ_i = cos(60°) = 0.5, meaning that the angle between triangles that share a boundary edge is greater than 26° and the angle between triangles that share a non-boundary edge is greater than 60°.

Highlights

- "Boundary-first" deformable modeling with medial axis representation is described.
- This paradigm enables segmentation of structures with branching medial geometries.
- The aortic valve apparatus is segmented in 3D echocardiographic images.
- Segmentation with deformable medial modeling is compared to manual analysis.
- Deformable medial modeling of both normal and pathological aortic valves is shown.

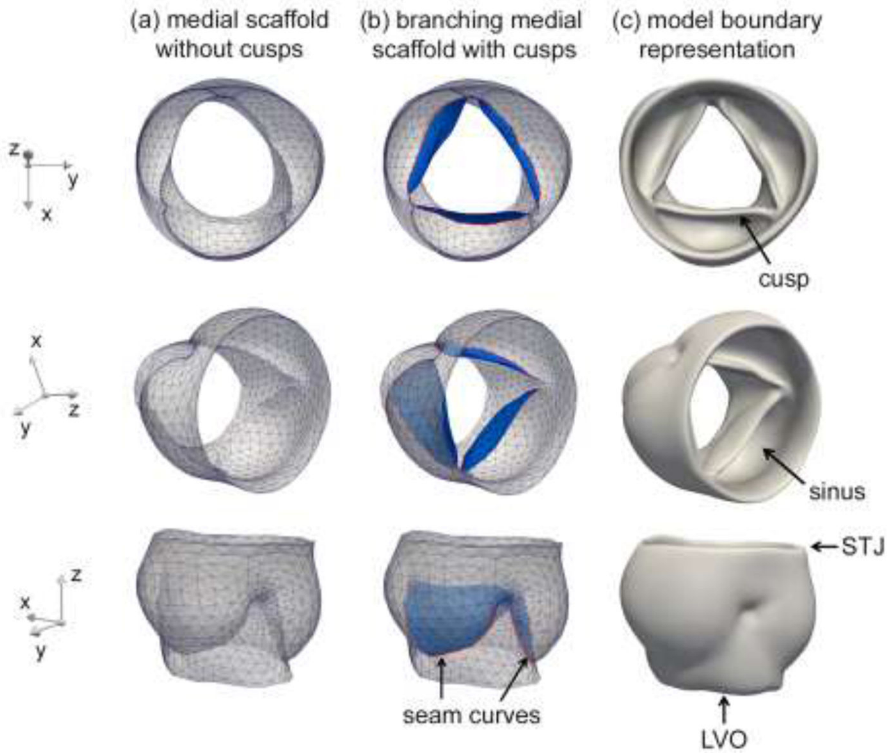

Figure 1.

(a) Medial scaffold of the aortic root without cusps viewed from three different perspectives. (b) Medial scaffold of the complete aortic valve complex, where the attachment sites of the cusps are seam curves in the medial scaffold. (c) Boundary representation of the aortic valve complex. (STJ = sinotubular junction, LVO = left ventricular outlet)

Author Manuscript
Author Manuscript
Author Manuscript

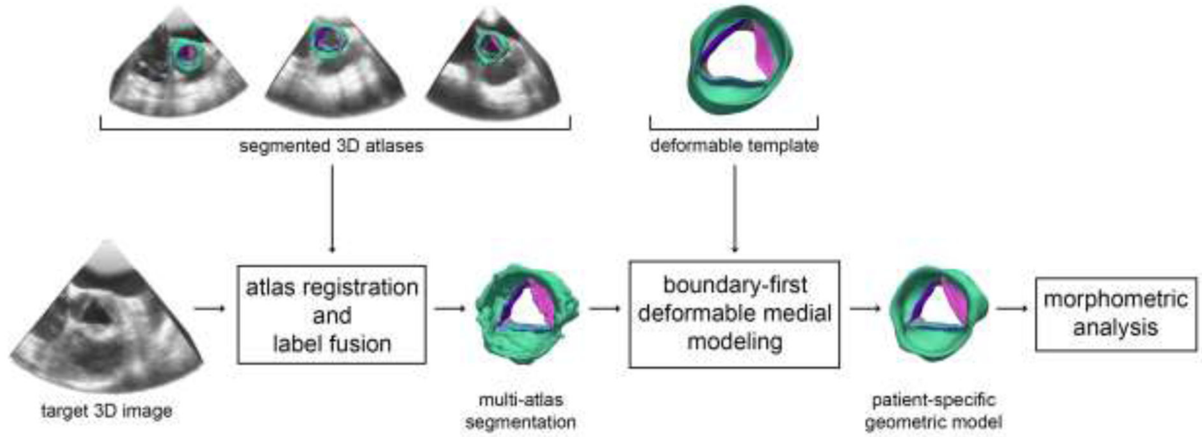

Figure 2.
Schematic of segmentation and deformable medial modeling of the aortic valve apparatus.

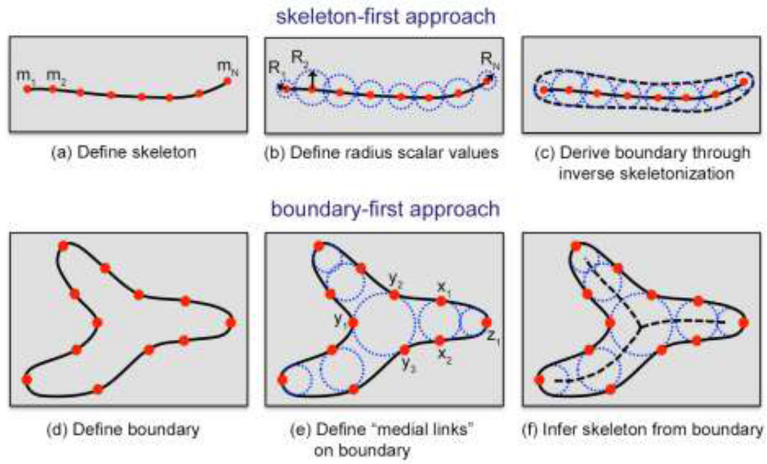

Figure 3.

(a–c) Skeleton-first approach and (d–f) boundary-first approach to deformable medial modeling.

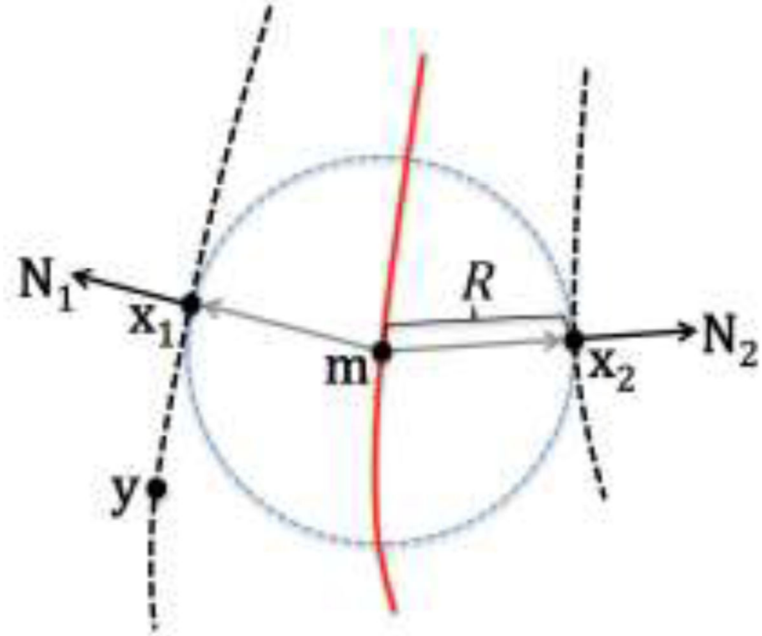

Figure 4.

Medial axis geometry shown in 2D for illustrative purposes. The dashed black curves demarcate the object boundary, the red curve is the object's medial axis, and the blue circle is a maximally inscribed disk centered at **m** with radius *R*. The disk is tangent to the boundary at $\mathbf{x_1}$ and $\mathbf{x_2}$. $\mathbf{N_1}$ and $\mathbf{N_2}$ are the outward normal vectors to the boundary at $\mathbf{x_1}$ and $\mathbf{x_2}$, and **y** is a point on the object's boundary.

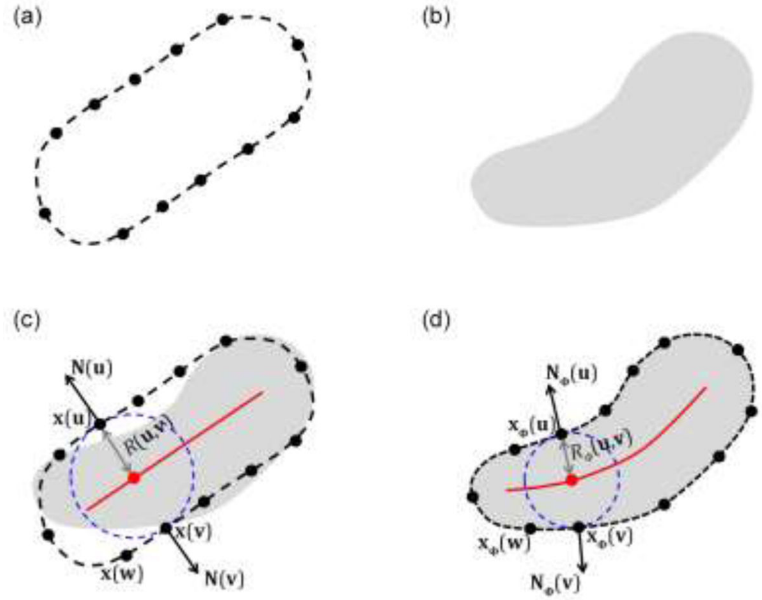

Figure 5.

(a) Template of an object's boundary, (b) target shape, (c) template overlaid on the target shape with medial axis notation, (d) template deformed to the target shape.

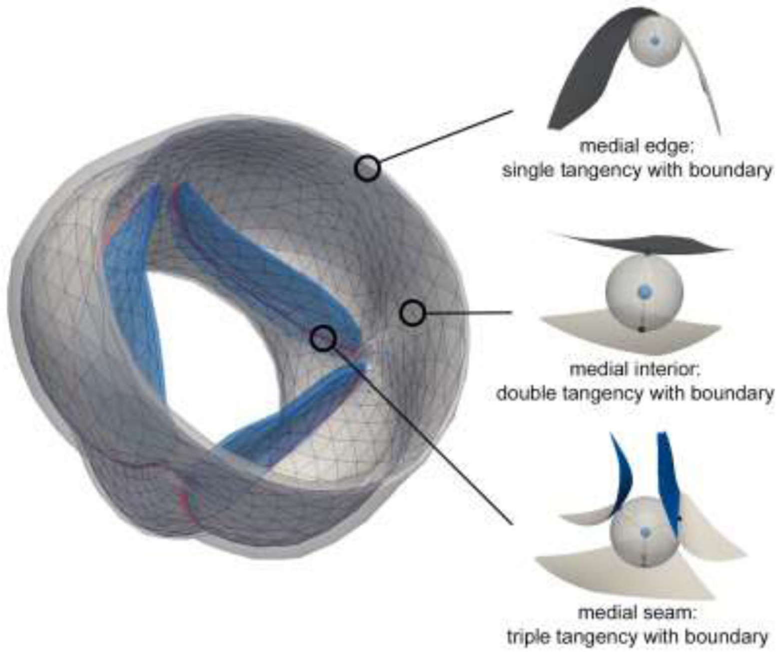

Figure 6.
3D medial geometry of the aortic valve apparatus, illustrating that maximally inscribed balls centered on the edges, interior, and seams of the medial axis have one, two, or three points of tangency with the boundary, respectively.

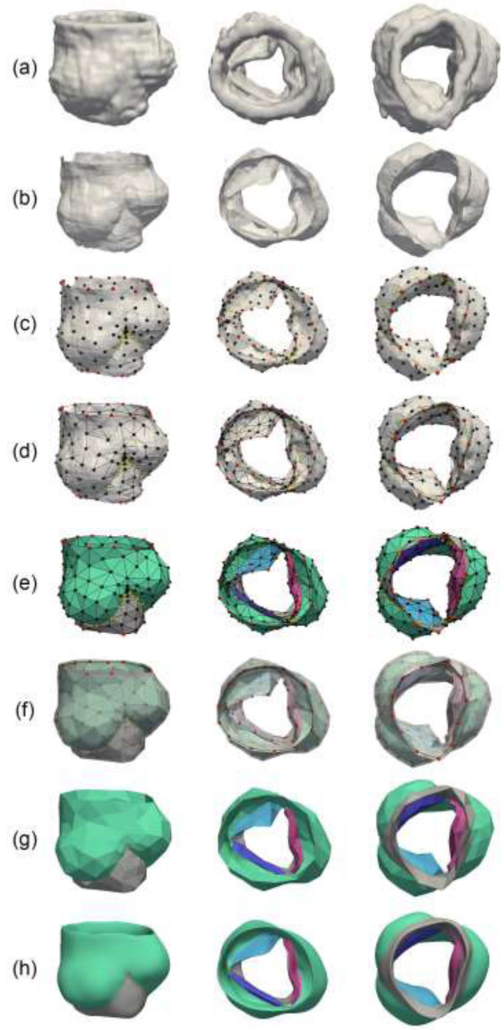

Figure 7.

The boundary template generation process illustrated from three viewpoints: a side view (left column), aortic view (center column), and ventricular view (right column). (a) Manual segmentation of the aortic valve apparatus. (b) Voronoi skeleton of the manual segmentation. (c) User-selected points on the skeleton. Edge, internal, and branch nodes are shown in red, black, and yellow, respectively. (d) Manual triangulation of the selected points. (e) Triangulated skeleton showing anatomical labels in color: left coronary cusp (blue), non-coronary cusp (purple), right coronary cusp (pink), sinuses (green), ventricular outflow segment (gray). (f) Inflated boundary shown in translucent gray superimposed on the triangulated skeleton mesh. (g) Coarse boundary mesh with anatomical labels shown in color. (h) Loop subdivided boundary mesh with the anatomical labels shown in color.

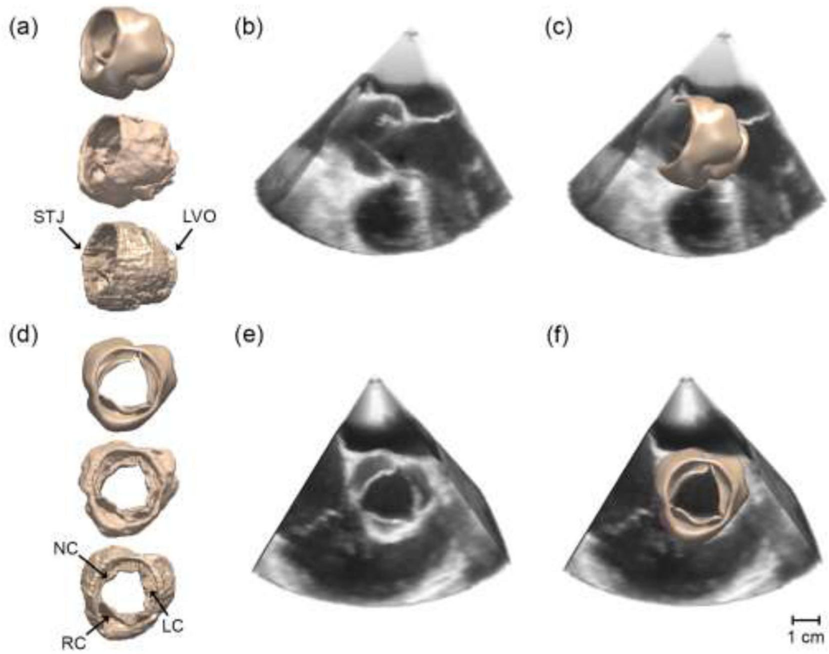

Figure 8.

(a) A fitted deformable model (top), multi-atlas segmentation (middle), and corresponding manual segmentation (bottom). (b) Grayscale 3DE image from which the model was generated. (c) Deformable model superimposed on the 3DE image. (d–f) Same as (a–c), but visualized from an aortic perspective.

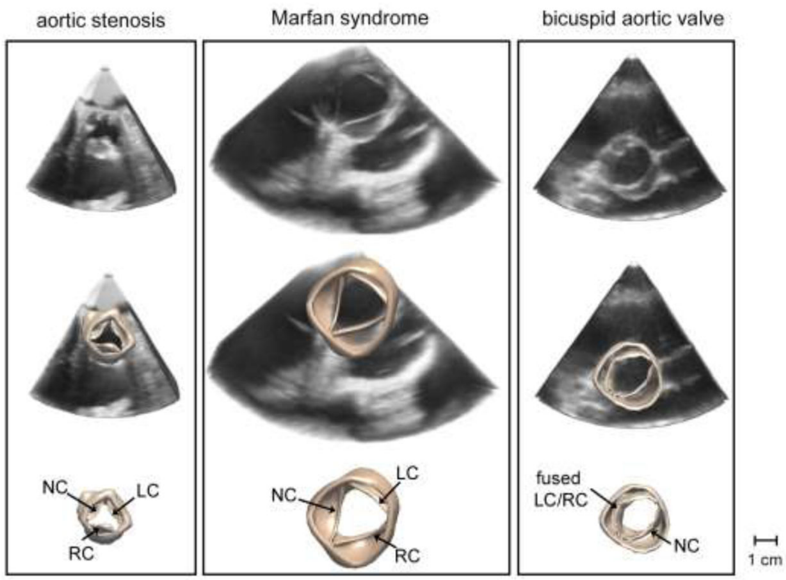

Figure 9.
Deformable medial models of diseased aortic valves. (NC = non-coronary cusp, LC = left coronary cusp, RC = right coronary cusp)

Table 1

Accuracy of image segmentation with deformable medial modeling based on the symmetric mean boundary error metric.

mesh comparison		mean boundary error (mm)	mean 95th percentile boundary error (mm)
mesh 1	**mesh 2**		
deformable model fitted to multi-atlas segmentation	manual segmentation	0.41 ± 0.10	0.89 ± 0.28
multi-atlas segmentation (no model fitting)	manual segmentation	0.32 ± 0.13	1.01 ± 0.62
deformable model fitted directly to manual segmentation	manual segmentation	0.23 ± 0.08	0.50 ± 0.08
deformable model fitted to multi-atlas segmentation	multi-atlas segmentation	0.22 ± 0.04	0.52 ± 0.07
deformable model fitted to multi-atlas segmentation	deformable model fitted to manual segmentation	0.36 ± 0.13	0.87 ± 0.26

Table 2

Measurements derived from the deformable medial model fitted to the results of multi-atlas segmentation (second column) and fitted to the results of manual segmentation (third column).

Measurement	Automated	Manual	Bias	Limits of Agreement	R
STJD	28.2 ± 3.0 mm	28.3 ± 3.2 mm	−0.2 mm	−1.0 to 0.7 mm	0.99
STJA	6.28 ± 1.38 cm^2	6.33 ± 1.47 cm^2	−0.05 cm^2	−0.45 to 0.35 cm^2	0.99
ASD	37.2 ± 3.5 mm	37.2 ± 3.5 mm	0.1 mm	−0.85 to 0.96 mm	0.99
ASA	10.82 ± 2.04 cm^2	10.81 ± 2.04 cm^2	0.01 cm^2	−0.53 to 0.55 cm^2	0.99
VOA	3.07 ± 0.60 cm^2	3.02 ± 0.60 cm^2	0.05 cm^2	−0.14 to 0.25 cm^2	0.99
AAD	25.2 ± 2.2 mm	25.3 ± 2.10 mm	−0.1 mm	−0.8 to 0.6 mm	0.99
AAA	5.00 ± 0.85 cm^2	5.03 ± 0.80 cm^2	−0.04 cm^2	−0.31 to 0.24 cm^2	0.99
LVOD	24.9 ± 2.6 mm	25.0 ± 2.9 mm	−0.1 mm	−1.6 to 1.5 mm	0.96
LVOA	4.88 ± 1.04 cm^2	4.91 ± 1.15 cm^2	−0.03 cm^2	−0.69 to 0.63 cm^2	0.96
SALC	2.34 ± 0.41 cm^2	2.53 ± 0.44 cm^2	−0.19 cm^2	−0.68 to 0.31 cm^2	0.82
SANC	2.34 ± 0.49 cm^2	2.53 ± 0.46 cm^2	−0.19 cm^2	−0.57 to 0.20 cm^2	0.91
SARC	2.80 ± 0.49 cm^2	2.83 ± 0.49 cm^2	−0.03 cm^2	−0.40 to 0.34 cm^2	0.93
TLC	1.9 ± 0.3 mm	2.0 ± 0.4 mm	−0.10 mm	−0.5 to 0.3 mm	0.80
TNC	1.6 ± 0.2 mm	1.7 ± 0.3 mm	−0.07 mm	−0.4 to 0.3 mm	0.74
TRC	1.9 ± 0.2 mm	2.0 ± 0.3 mm	−0.05 mm	−0.4 to 0.3 mm	0.79
TSV	2.2 ± 0.3 mm	2.3 ± 0.3 mm	−0.12 mm	−0.5 to 0.3 mm	0.75

Table 3

Measurements derived from the deformable medial models of pathological aortic valves.

Measurement	Marfan syndrome	Aortic stenosis	Bicuspid valve
STJD	37.4 mm $^{(++)}$	21.8 mm $^{(--)}$	34.6 mm $^{(++)}$
STJA	10.86 $cm^{2\,(++)}$	3.68 cm^2	9.41 $cm^{2\,(++)}$
ASD	52.5 mm $^{(++)}$	32.4 mm	39.1 mm
ASA	21.46 $cm^{2\,(++)}$	8.14 cm^2	11.92 cm^2
VOA	6.96 $cm^{2\,(++)}$	1.50 $cm^{2\,(--)}$	4.81 cm^2
AAD	35.8 mm $^{(++)}$	21.8 mm	29.9 mm $^{(++)}$
AAA	9.41 $cm^{2\,(++)}$	3.75 cm^2	6.76 cm^2
LVOD	33.3 mm $^{(++)}$	21.4 mm	28.0 mm $^{(++)}$
LVOA	8.43 $cm^{2\,(++)}$	3.59 cm^2	5.98 cm^2
SALC	4.34 $cm^{2\,(++)}$	1.67 cm^2	—
SANC	3.82 $cm^{2\,(++)}$	1.28 $cm^{2\,(--)}$	4.05 $cm^{2\,(++)}$
SARC	5.61 $cm^{2\,(++)}$	1.77 $cm^{2\,(--)}$	—
TLC	2.0 mm	1.2 mm $^{(--)}$	—
TNC	1.3 mm $^{(--)}$	1.5 mm	1.9 mm
TRC	1.9 mm	2.4 mm $^{(++)}$	—
TSV	2.6 mm	2.9 mm $^{(++)}$	2.6 mm